University of California
Santa Barbara

Influence of Multi-cycle Loading on Structure and Mechanics of Marine Mussel Plaques

A thesis submitted in partial satisfaction
of the requirements for the degree

Master of Science
in
Mechanical Engineering

by

Menaka Wilhelm

Committee in charge:

Professor Megan T. Valentine, Chair
Professor Robert M. McMeeking
Professor J. Herbert Waite

June 2017

The Thesis of Menaka Wilhelm is approved.

Professor Robert M. McMeeking

Professor J. Herbert Waite

Professor Megan T. Valentine, Committee Chair

June 2017

Influence of Multi-cycle Loading on Structure and Mechanics of Marine Mussel Plaques

by

Menaka Wilhelm

Acknowledgements

This work was supported by the MRSEC Program of the National Science Foundation under Award No. DMR 1121053.

I'm grateful for many useful discussions with Danny DeMartini, Emma Filippidi, and the members of my thesis committee. Mark Cornish provided invaluable technical assistance in microscopy.

Abstract

Influence of Multi-cycle Loading on Structure and Mechanics of Marine Mussel Plaques

by

Menaka Wilhelm

The proteinaceous byssal plaque-thread structures created by marine mussels exhibit extraordinary load-bearing capability. Although the nanoscopic protein interactions that support interfacial adhesion are increasingly understood, major mechanistic questions about how mussel plaques maintain toughness on supramolecular scales remain unanswered. This study explores the mechanical properties of whole mussel plaques subjected to repetitive loading cycles, with varied recovery periods. Mechanical measurements were complemented with scanning electron microscopy to investigate strain-induced structural changes after yield. Multicyclic loading of plaques decreases their low-strain stiffness and introduces irreversible, strain-dependent plastic damage within the plaque microstructure. However, strain history does not compromise critical strength or maximum extension compared with plaques monotonically loaded to failure. These results suggest that a multiplicity of force transfer mechanisms between the thread and plaque-substrate interface allow the plaque-thread structure to accommodate a wide range of extensions as it continues to bear load. This improved understanding of the mussel system at the micron-to-millimeter lengthscale offers strategies for including similar fail-safe mechanisms in the design of soft, tough and resilient synthetic structures.

Contents

Chapter 1

Introduction

In their native intertidal environment, sessile marine mussels, *Mytilus californianus*, routinely contend with crashing waves, tidal ebb and flow, and predators. By depositing a radial array of acellular plaque-tipped threads, called the byssus, each mussel creates its own anchor. Each plaque-thread structure can be viewed as a multicomponent composite: the proximal portion of the thread is shielded within the mussel shell interior and connects to the exposed distal portion of the thread, which in turn interpenetrates an elliptical, thin-film adhesive plaque [1]. A tough outer cuticle covers the plaque core and distal thread [2], and the result is a leathery adhesive structure that adheres strongly to a variety of soft and hard substrates [3].

The remarkable ability of the plaque-thread structure to adhere to wet, fouled, salt-encrusted and corroded surfaces has motivated the study of the interfacial adhesive proteins at the plaque-substrate interface. There is increasingly comprehensive knowledge of how the mussel foot proteins (mfps) provide hydrogen and metal ion coordination bonding via the abundant catecholic side groups of 3,4-dihydroxyphenyl-L-alanine (DOPA), while contributing to cohesive strength by catechol oxidase-mediated protein cross-linking [4][5]. Similarly, the extensibility and self-healing properties[6] of the distal portion of

the byssus thread have prompted examination of chemical gradients [7] and metal coordination [8] within the collagen-rich thread. These efforts have improved our knowledge of how dynamic bonding and force-induced bond rupture contribute to toughness at the molecular level.

Despite the crucial role that the plaque plays as an intermediary between the collagen thread and the interfacial adhesive proteins, the mechanical contributions of the bulk plaque interior are much less understood. Beneath the cuticle coating, the plaque core exhibits a fiber-reinforced cellular structure, consisting of a network of pores [9] with heterogeneous interpenetration of long collagen bundles that connect back to the distal collagen thread. Previously reported fracture toughness of a plaque connected to 2 cm of distal thread [10] indicates that the bulk plaque can dissipate energy to provide cohesive strength. Rate-independent mechanical behaviour of adhered plaques [10] measured in the range of 0.6 to 180 μm/s suggests that supramolecular mechanisms which function at longer length scales than the previously studied nanoscale molecular bonds play a role in plaque cohesion and strength. However, the nature of how micro- and mesoscopic mechanisms and structures contribute to cohesive strength and bulk toughening in the plaque is not known.

In order to investigate how repeated loading of the plaque affects stiffness, strength, and microstructure, this study couples mechanical characterization of repeated loading-unloading cycles, which result in hysteretic behavior, with imaging of strain-dependent microstructural changes in the plaque core as assessed via electron microscopy. Repeated loading cycles result in extension-dependent hysteresis of the force response. Plaque-thread structures subjected to repeated extension exhibit a decrease in small strain stiffness, which is accompanied by void formation in the porous bulk matrix, slippage at the fiber-foam interface, and fracture of the matrix and/or fibers. Although the plaque sustains several forms of microstructural damage, and in some cases, partial delamina-

tion from the underlying substrate, the material strength remains comparable to that of monotonically loaded plaques with no cyclic strain history.

Chapter 2

Methods

2.1 Mussel Plaque Collection

Mussels (*Mytilus californianus*; Conrad, 1837) were collected from the fishing pier (34.415605, -119.828911) on the coast of Goleta, CA and placed in shallow tanks with continuously circulated and aerated raw seawater at temperatures ranging from 9°C to 14°C. To enable the collection of plaque-thread samples for testing, mussels were tethered via large rubber bands to acrylic plates tiled with glass slides (each 75 mm × 25 mm). Every 3-5 days, all plaques deposited onto the glass-slide substrates were collected, following which the mussels were repositioned over fresh slide-coated surfaces to continue their deposition of plaques. Once collected, plaques were rinsed with Milli-Q water and stored at 4°C for 1-24 days. These studies used a total of 60 plaques harvested from 9 mussels. The plaque-producing mussels were between 8.5-14.5 cm long.

2.2 Mechanical Testing

Mechanical testing was performed as previously described [10]. Briefly, a custom-built load frame combines a digital stepper motor, an analog force sensor, and a microscope for imaging the plaque:glass interface from below. Force, extension, and imaging data were collected at 10Hz, 20Hz, and 10Hz, respectively. Force and extension measurements were down-sampled to 2.5Hz by binning measurements from each device in a 0.4s window and taking their average, to minimize the effects of small offsets in data collection start times and to ensure that images could be correlated to the force and extension measurements.

To enable secure attachment of glass-slide-bound plaque to the motor, the thread was glued to a 1-mm diameter glass rod (Sutter Instrument, 415-883-0128) using a polyurethane-based waterproof glue (Gorilla Glue). A short segment (2mm) of free thread remained between the plaque and rod in all cases. The plaques were left to dry overnight then rehydrated in MilliQ water for at least 10 minutes before testing. The glass rod was then secured to the motor at an angle of 45° and the plaque was pre-loaded to a measured force of 0.6N to eliminate slack in the thread. In all cases, a loading rate of 30 μm/s, or 1.8 mm/min, was used. For all loading and recovery periods the plaques remained submerged in Milli-Q water. Testing in Milli-Q water, rather than highly oxidative seawater, improved repeatability of experiments.

Previous work showed that plaque detachment force scaled linearly with plaque diameter D_p [10]. The geometric mean of the diameters of the elliptical plaque's major-dimension, D_M, and minor-dimension, D_m, was calculated as follows: $D_p = \sqrt{D_M * D_m}$. This allowed the measured detachment force, F, to be normalized to account for variations in plaque diameters: $F^* = F \times (\frac{2.5}{D_p})$ where 2.5 mm was the mean diameter of all plaques tested.

Monotonically loaded samples were pulled to failure. As is common in soft-materials

testing, many samples failed due to stress concentrations associated with gluing the end of the thread. Samples that failed at the plaque typically failed by loss of adhesion at the plaque-glass interface, although internal cohesive failure was also sometimes observed, in agreement with prior studies [10].

Cyclic tests were informed by the yield observed in monotonic tests. The approach to yield was monitored through calculation of the force difference measured between successive motor steps. In cyclic loading, plaques were first pulled until this force difference dropped below a threshold set to 5mN, indicating exit from the linear response regime. We call the extension corresponding to this force threshold Δx_y. The plaques were then unloaded fully, and pulled to $2\Delta x_y$ then unloaded to zero extension again, and pulled next to $4\Delta x_y$. In the fourth and final cycle, the plaques were loaded to failure (Table 1). All cyclic tests were extension-controlled.

2.3 F-X Curve Analysis

To determine the extent of the initial linear elastic range, we used a custom-written, semi-automated fitting routine implemented in MATLAB. For each loading curve, the fit was manually initialized with two inputs: the maximum range of extensions over which the force-displacement data should be fit, and one anchor point that must be included in the final fit. The program then iteratively performed linear fits over all possible ranges of points that included the anchor point within the maximum range. Any range containing less than 2 sec of measured data was discarded. Of the ranges that contained sufficient data, we selected the range with maximum R-squared value, and used this as the final linear fit. The linear fits were not forced through zero, and the zero-force extension (x-intercept) of the final fit was subtracted from the extension data. To determine the transition between linear loading and non-linear yield, we compared the expected force

value which was predicted from the fit to the measured force at each value of extension. We defined the proportional limit threshold as the point where the difference between the expected and measured force values exceeded 5mN. The proportional limit has associated extension, Δx_{PL}, and force, F_{PL} parameters.

2.4 Scanning Electron Microscopy

Scanning electron microscopy was used to image the internal structures of the mussel plaques, as described [9]. Briefly, plaques were fixed for 4 hours in a solution of 3.7% formaldehyde and 2.5% glutaraldehyde in water. Following fixation, the plaques were stored in Milli-Q water at 4°C for 1-3 days. Each plaque was then embedded in Neg-50 cryoprotectant (Thermo Scientific) and sectioned at -21°C (Leica CM 1850) to create 20 μm thick slices parallel to the direction of the thread (along the long axis of the elliptical plaque) that were immediately placed in Milli-Q water. All sections were rinsed repeatedly to remove cryoprotectant, then taken through several rounds of solvent exchange from water to ethanol using ratios of water:ethanol as follows: 3:1, 1:1, 1:3, 1:9, 0:1. Sections were rinsed three times with ethanol to ensure no water remained, then exchanged from ethanol to hexamethyldisilazane (HMDS, CAS 999-97-3) using ratios of ethanol:HMDS of 2:1, 3:2, 1:2. Samples were mounted on aluminum microscopy stubs using carbon adhesive, and sputter coated for 90 s with gold/palladium 60/40 99.99% (Hummer 6.2, Anatech, USA). Imaging was performed with the FEI Nova NanoSEM at an accelerating voltage of 5 kV. Experiments for each condition were performed in triplicate.

Chapter 3

Mechanical Behavior

3.1 Monotonic Loading to Failure

We first tested the force response of individual thread-plaques that were monotonically loaded to failure at a pull angle of 45° and a loading rate of 30 μm/s. In each case the same general features were observed: an initial elastic regime, followed by a yield region, and an eventual increase in force at large extensions comparable to or exceeding the unloaded thread length (Figure 3.1). Although the individual age and size of each mussel influenced the plaque properties, we found that scaling by the plaque's geometric mean and normalizing by the proportional limit collapsed the data and allowed for comparison between different mussel samples.

The irregular and variable geometry of the thread-plaque samples prevented the straightforward conversion of our mechanical data, which is collected as force and extension as functions of time, to stress and strain. Thus, the small-displacement stiffness was determined from a linear fit of the force-displacement curve, with a maximum linear extension that did not exceed 0.3mm. Given our thread length of ∼2mm and the low height profile of the adhered plaque (100-200μm), we estimate that this value cor-

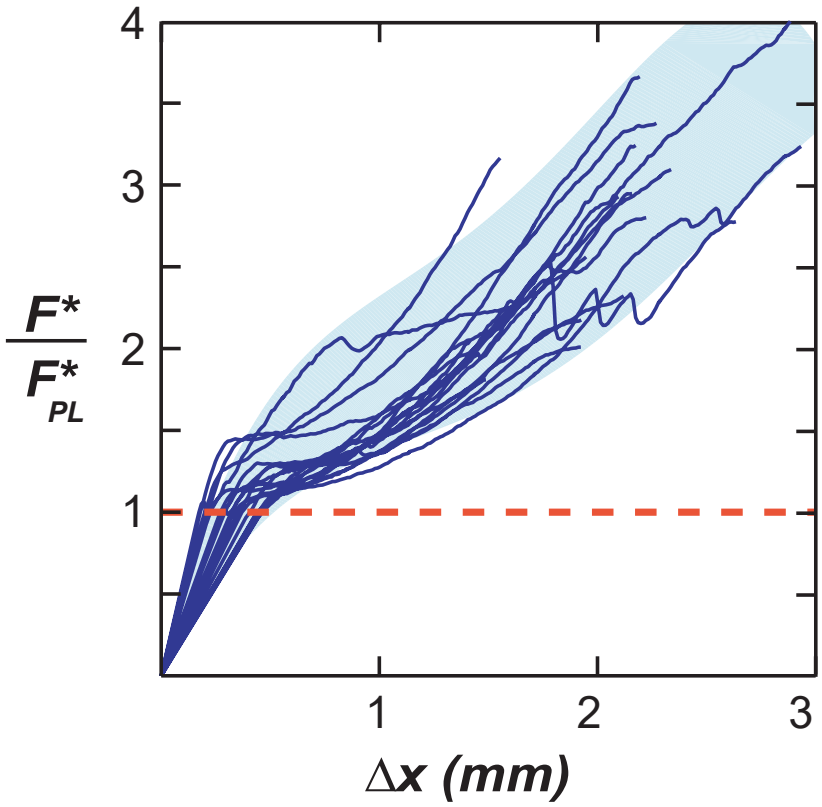

Figure 3.1: The force required to extend the thread-plaque sample in monotonic loading. The force response for individual thread-plaques varies among different mussels, but the curves largely collapse when normalized by the proportional limit of force (number of plaques, n=18, derived from 9 different mussels). Each curve displays the same general features: an initial linear regime, followed by a yield region, and an eventual increase in force at large extensions. The dotted line indicates the transition from the linear regime to the yield region for each sample. The shaded area indicates the range of the monotonic loading data. This range was created by manually selected points to create maximum and minimum bounds of the envelope, then fitting these respective series of points to a 4th order polynomial function.

responds to approximately 10% strain in the structure. The linear stiffness serves as a proxy for the elastic modulus, and the maximum force measured for a given loading cycle is interpreted as the sample strength.

One important difference between the current study and previous mechanical tests of adhered plaques [10] is a reduction in the length of the exposed thread that is allowed

to contribute to load transmission from 20mm in prior work to 2mm here. Interestingly, in both cases, similar force responses and failure modes were observed. Onset of yield occurred at extensions of ∼10% of the total thread length and the forces associated with this yield ranged from 0.25N to 1.5N. Structural failure or detachment occurred at extensions of ∼30-50% of total thread length in the case of the 2-cm long thread and at extensions of ∼100% thread length for the 2-mm length thread. Maximum forces were extremely similar, ranging from 1N to 4N in the 2-cm thread case and from 0.5 N to 3 N in the 2-mm thread case, despite the 10-fold reduction in thread length. This suggests some role for the plaque, independent of the thread, in determining the critical extension and force at failure. It is possible that chemical gradients known to exist within the thread [7] play a role, resulting in stronger contributions to load-bearing in the portion of the thread closest to the plaque. Also, there are differences in the hydration state of the plaque during processing and measurement between this and prior studies. In the current study, we included an overnight drying step to allow the short thread to be securely glued to a glass rod connected to the motor. As the mussel thread and plaque naturally encounter drying and rehydration in the intertidal zone [11], we expect effects due to drying to be minimal. During measurement, the plaque and 2-mm thread were completely submerged. Previously, in the 2-cm thread case, there was no overnight drying step, and during the measurement the thread was partially hydrated by misting but was not submerged. These differences may play a role in determining the maximum thread extension as well.

3.2 Multi-cycle Loading

We next investigated the response of thread-plaque structures to extension-controlled multicyclic loading. After confirming that cyclic loading within the linear regime resulted

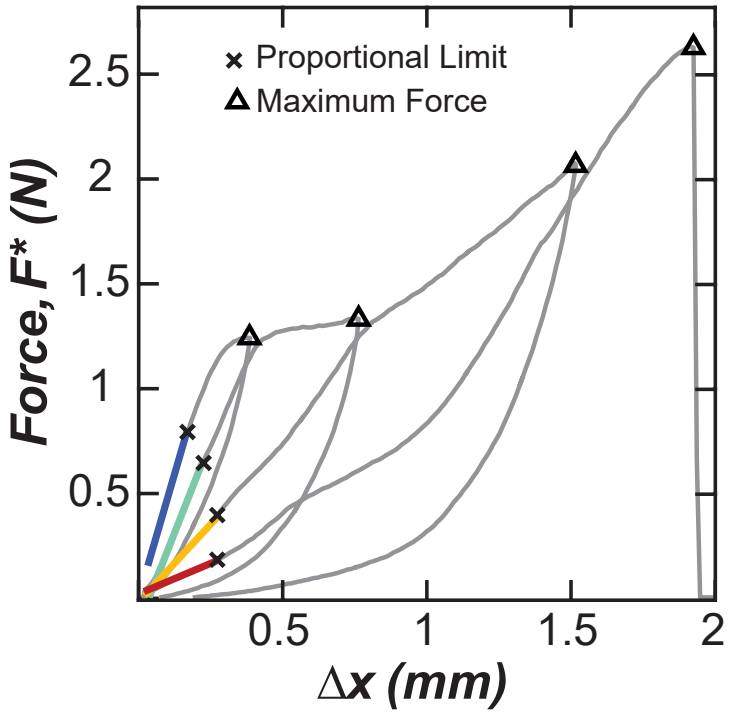

Figure 3.2: The force-extension curve for a representative cyclic loading experiment. The small-strain stiffness fit for each loading curve is shown in a different color (cycle 1 in blue, cycle 2 in cyan, cycle 3 in gold, and the final load to failure in red). For each cycle the peak force (open triangles) and the proportional limit (X-mark) is shown.

in reversible unloading-loading behavior with minimal hysteresis (data not shown), we designed the extension-controlled load cycles as summarized in Table 1.

For each sample, a similar overall mechanical response was observed (Figure 3.2). For each cycle that loaded the thread-plaque into the yield domain, we observed hysteresis between the loading and unloading curves, consistent with the action of a toughening mechanism that dissipates the applied stress and prevents large scale crack propagation and brittle failure. The dissipated energy, which can be approximated by the enclosed area within the hysteretic loop, increased with each loading cycle to greater extension.

Cycle	1	2	3	4
Loaded to:	Yield, Δx_Y	$2\Delta x_Y$	$4\Delta x_Y$	Failure
Unloaded to:	$\Delta x_Y = 0$	$\Delta x_Y = 0$	$\Delta x_Y = 0$	None

Table 3.1: Summary of extension-controlled load cycles.

The sample stiffness was determined from the initial slope of the force-extension curve for each cycle. With each loading, the stiffness decreased, indicating that at least some of the observed toughening arises from irreversible plastic mechanisms that compromise the small-strain elasticity (Figure 3.4). We observed a modest stiffness decrease of $\sim$10% in cycle 2, as compared with the first loading. When the samples were extended into the non-linear regime, the stiffness decreased further. By the third loading the stiffness was typically reduced to $\sim$50% of its original value, and by cycle 4 the stiffness was only $\sim$20% of its original value.

The nonlinear force-extension response also depended on the previously applied maximum extension. For applied extensions exceeding the maximum of the previous cycles, the force extension response upon loading closely resembled that of pristine samples that were monotonically loaded to failure. In contrast, for extensions that were less than the previous maximum value, the force response was consistently lower than that measured in the initial pull but higher than the forces developed in the prior unloading. Such dependence of the nonlinear mechanical response on the prior loading history is common in a wide range polymeric samples, including elastomers [12] and hydrogels [13]. However, in contrast to the classic Mullins effect [14], the reloading curves do not follow the previous unloading curve exactly, indicating some level of molecular recovery when the pulling force is reduced.

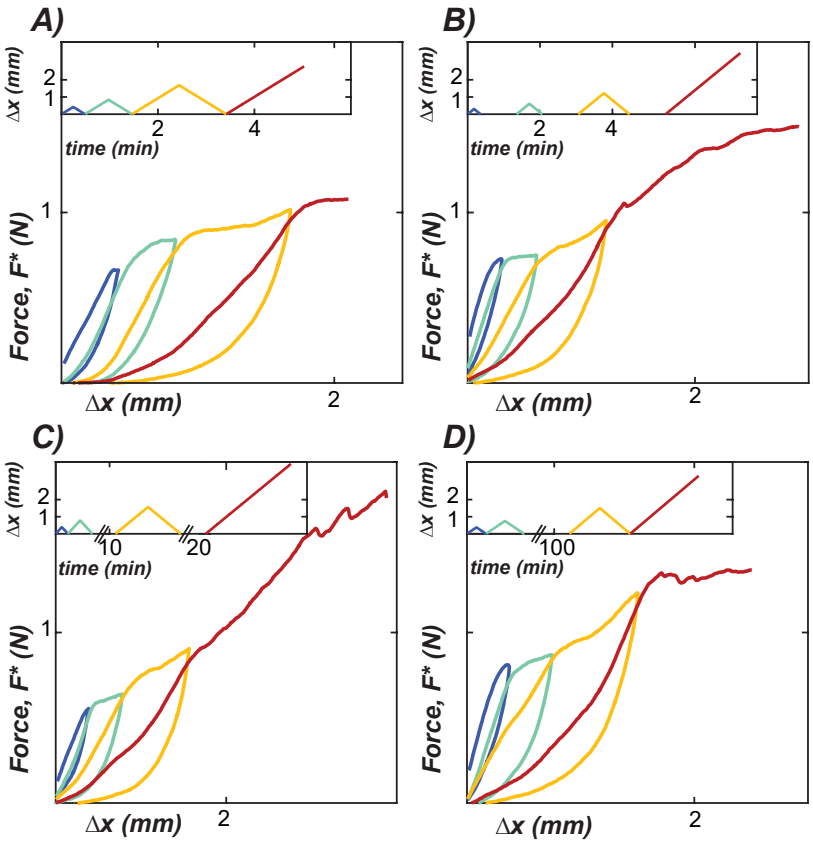

Figure 3.3: Representative force-extension curves for the extension-controlled cyclic loading tests. Each panel shows a typical force-extension curve performed with: (A) no recovery time, (B) 1 minute of recovery between each loading and unloading period, (C) No recovery between cycles 1 and 2, 10 minutes of recovery between cycles 2 and 3, and between cycle 3 and the final load to failure (D) 100 minutes of recovery between cycles 2 and 3, but otherwise no recovery. Each load/unload cycle is shown in a different color (cycle 1 in blue, cycle 2 in cyan, cycle 3 in gold, and the final load to failure in red). In each panel the extension versus time is displayed as an inset.

3.3 Time-dependent Recovery

To further explore the ability of loaded mussel thread-plaque systems to recover their mechanical strength and properties after loading, we repeated the multicycle loading experiments using three different loading schemes: with 1 minute of recovery between each of the three loading and unloading periods (Figure 3.3B); with no recovery time between cycles 1 and 2, but 10 min of recovery between cycles 2 and 3 and between cycle

3 and the final load to failure (Figure 3.3C); and with 100 min of recovery between cycles 2 and 3, but otherwise no waiting time (Figure 3.3D). In all cases, we found the same general features as those observed with no recovery period between any of the cycles. To

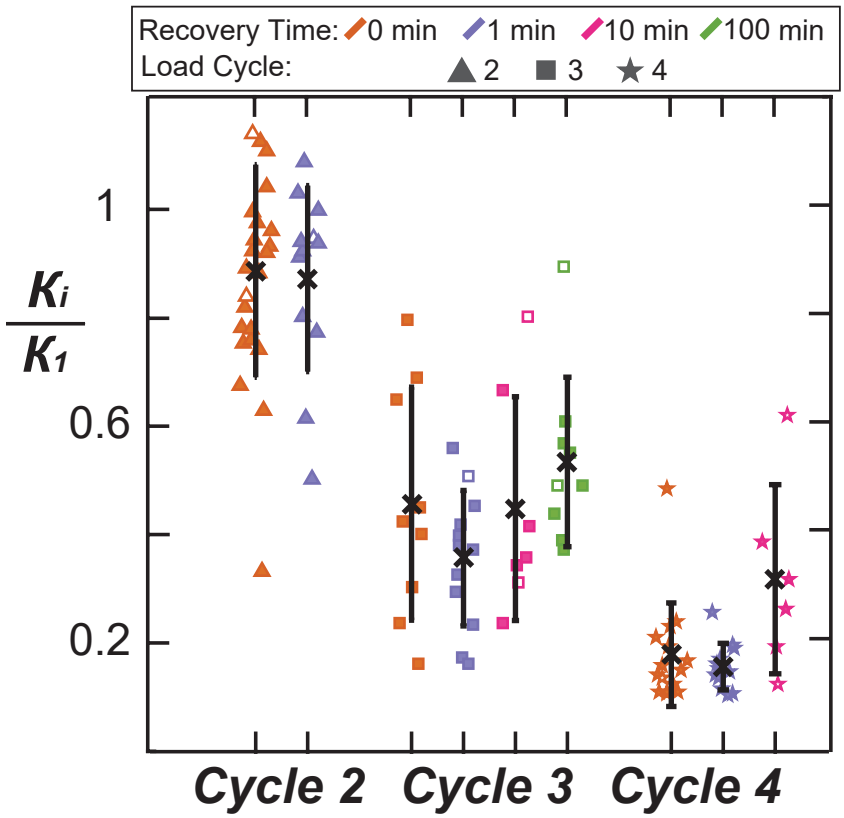

Figure 3.4: The change in small strain stiffness as a function of recovery time. Here, the change in small strain stiffness is calculated as the ratio of the stiffness measured during the i-th loading cycle to the initial small strain stiffness, measured during the first loading). Different colors show varying recovery times between the shown stiffness and the previous load cycle. The data points are slightly offset along the x-axis to improve readability. In all cases, the measured stiffness decreases when subjected to additional loading cycles, so the value is always less than 1. No strong evidence of recovery is found. An open symbol denotes a plaque that was partially delaminated at the proportional limit of the loading cycle; delamination appears to have little effect on the small strain stiffness.

assess the effect of waiting time on the linear force response, we compared the linear, small-strain stiffness measured in subsequent loading cycles, κ_i, to that of the initial

loading, κ_1, for a variety of waiting times. We found that in all cases the reduction in stiffness was similar to that measured when no waiting time was included between cycles (orange markers, Figure 3.4), and found no evidence of significant stiffness recovery for waiting times of up to 100 minutes (green markers, Figure 3.4). Interestingly, we did not observe a difference in the stiffness reduction between plaques that were fully adhered to the glass surface and plaques that had started to delaminate (compare solid and open symbols in Figure 3.4). This may suggest that the linear stiffness is dominated by bulk effects rather than the mechanics and load transfer properties of the interface.

To investigate how this repetitive loading affected plaque strength, we superimposed the normalized peak force measured from each loading cycle on the normalized range of force responses from plaques loaded monotonically (Figure 3.5). In most cases, progressive peak forces continued to rise in a manner that closely resembled the stiffening observed in the monotonic force response. Samples loaded with no recovery still exhibited peak forces which coincided with the range of force response in pristine samples, as did those with longer recovery periods (compare different colors, Figure 3.5). Additionally, plaques which showed partial delamination at the measured peak force maintained strength comparable to fully adhered samples (open symbols, Figure 3.5). These data suggest that strength of the plaque-thread structure is not affected by cyclic load history, or even partial delamination of the plaque.

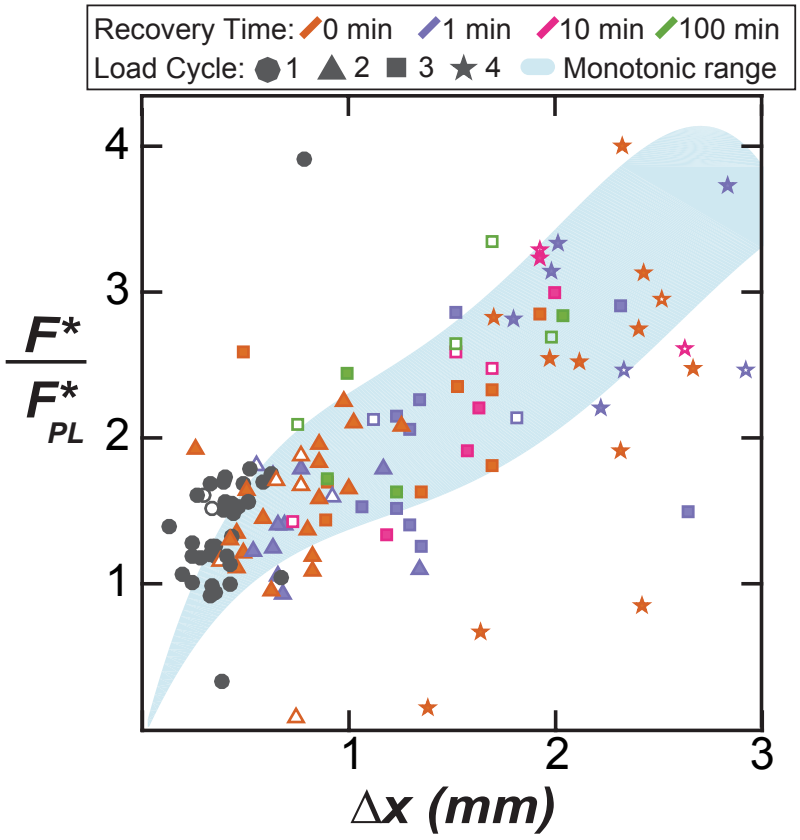

Figure 3.5: Peak forces measured in cyclic tests follow the monotonic loading curve, independent of load history and delamination. Here, the peak forces from all cyclic loading tests are compared with the range of monotonic force response. Different colors show the peak forces of loading cycles with different recovery times (no recovery time in orange, 1 min recovery time between each cycle in purple, 10 minutes recovery time between cycles 2 and 3 in pink, and 100 minutes recovery time between cycles 2 and 3 in green). Different shapes denote the loading cycle from which the peak force was extracted, as described in the inset. Open symbols show samples which were partially delaminated at the peak force measurement.

Chapter 4

Microstructure Analysis

Using electron microscopy, we investigated the extensions outlined in Table 1 for the onset of microstructural damage at the plaque core and exterior.

4.1 Bulk Plaque Interior

In control plaques that were not subjected to loading, the core of the plaque showed a cohesive porous network structure (Figure 4.1), with collagen thread interpenetration evident as darker bands throughout the foam (dashed plum ellipse), consistent with prior results [9]. At the internal interfaces where the foam meets the collagen thread, these two materials appeared completely connected (Figure 4.1A, light blue ellipse). Some amount of pore compression was evident within the bulk, particularly near the interface between the substrate and foam but no damage was evident (Figure 4.1C and 4.2F, light green).

At extension of $2\Delta x_y$, where the largest decrease in stiffness was observed, significant microstructural damage was evident (Figure 4.2). The fibrous network of collagen fibers appeared to have been pulled apart in some areas (Figure 4.1, lower right panel, plum ellipse), and delamination occurred at the collagen fiber-foam interface (Figure 4.2D,

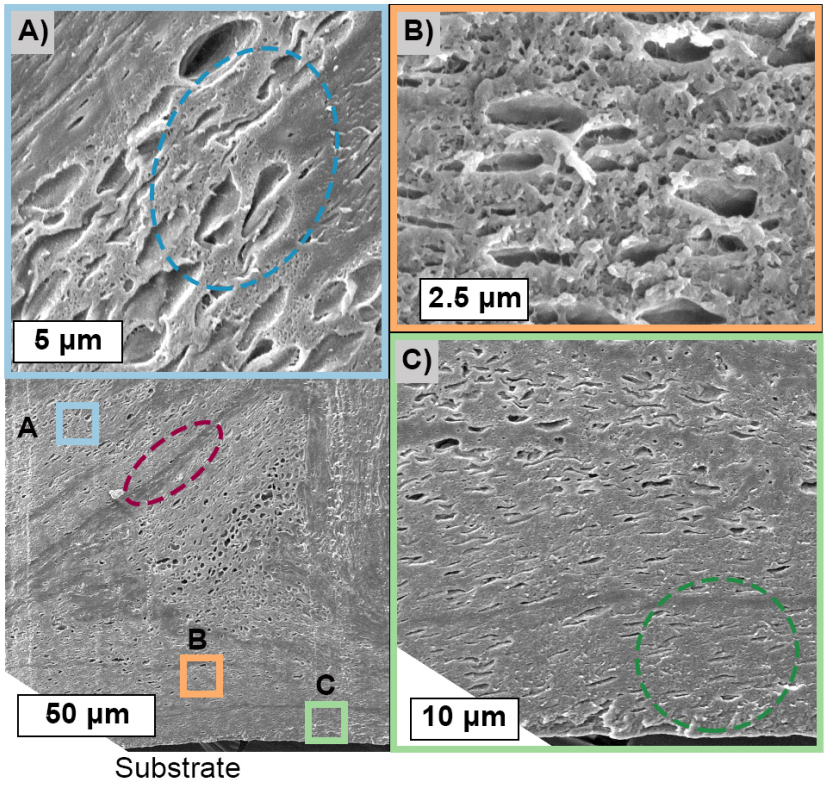

Figure 4.1: Internal microstructure of unstrained plaque. Each plaque is sectioned parallel to the direction of the distal thread, and lower left inset shows whole section view of respective samples. Dashed plum ellipse highlights where collagen interpenetrates the foamy structure. Three regions in each plaque are shown at higher magnification to allow microscale features to be more easily observed: (A)The thread-foam interface is intact (light blue dashed ellipse) in the unstrained sample. (B) The foam structure in the unstrained bulk shows pores with two length-scales. (C) Foam at the substrate edge is intact, and pores show some compression from circular entities to elliptical entities (dashed green circle).

dashed blue ellipse). In addition, large voids ripped open in the porous core (Figure 4.2E). Despite these structural changes, the porous foam at the interface remained unchanged (Figure 4.2F, dashed green ellipse), although this varied from sample to sample and in other mechanical tests delamination of plaques at similar extensions was observed. Plaques that were pulled to extension of $2\Delta x_y$ and allowed to recover for 100 minutes before imaging still exhibited many of the same microstructural changes evident in plaques

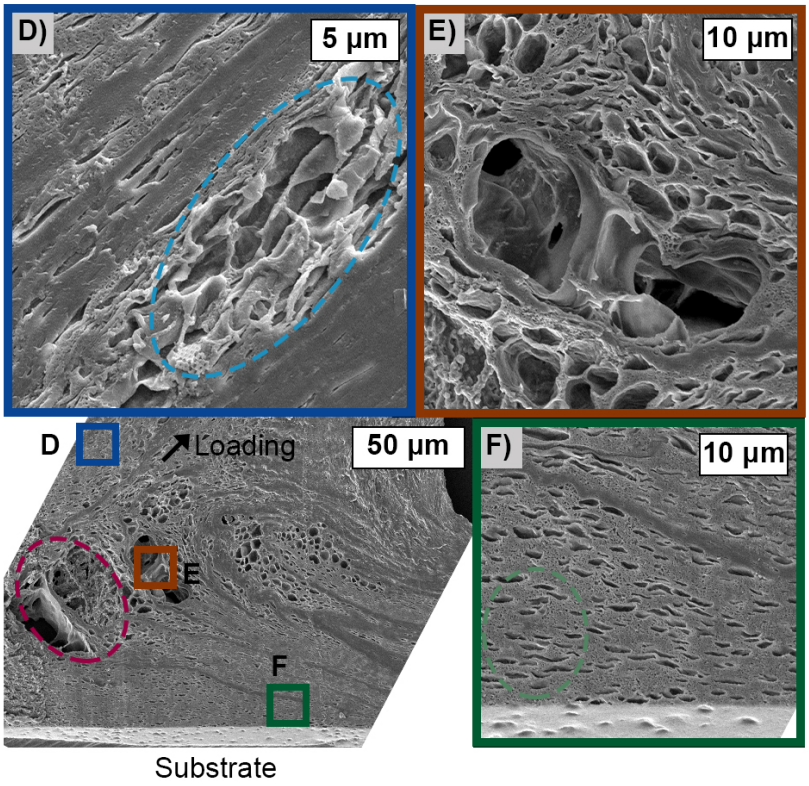

Figure 4.2: Internal microstructure of plaque strained to $2\Delta x_Y$. Each plaque is sectioned parallel to the direction of the distal thread, and lower left inset shows whole section view of respective samples. Dashed plum ellipse highlights where collagen interpenetrates the foamy structure. Three regions in each plaque are shown at higher magnification to allow microscale features to be more easily observed: (D) Delamination between the collagen thread and porous foam appears at the highest point of the foam (dashed blue ellipse). (E) Large voids form in the porous structure (F) In this case, the interface remains intact (dashed green ellipse).

fixed at strain with no recovery. The existence of this large scale, irreversible structural damage is consistent with the decreased small strain stiffness with multiple loading cycles, which also failed to recover after 100 minutes of waiting time (Figure 3.3). In contrast, external microstructure maintained integrity at $2\Delta x_y$.

4.2 Plaque Exterior

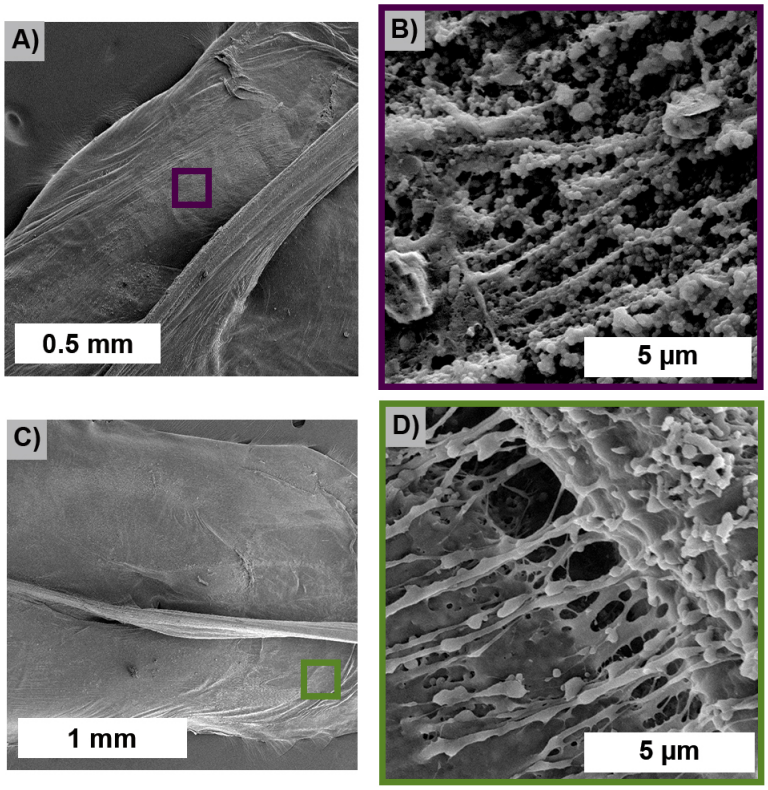

Figure 4.3: External microstructure of unstrained plaque compared to plaque strained to $4\Delta x_y$. (A) Whole plaque-thread structure of unstrained plaque, view from above. (B) Bands of cuticle granules appear dense and undamaged. (C) Whole plaque-thread structure of plaque strained to $4\Delta x_y$. (D) Fibrils thin and stretch apart under strain.

At $4\Delta x_y$, where low-strain stiffness dropped to ∼20% of initial stiffness, external microstructural damage was observed. Prior to this extension, no significant changes to plaque exterior were observed (Figure 4.3). Plaques extended to $4\Delta x_y$ exhibited separation and thinning of bands of granules of the cuticle coating, which extends from the thread over much of the plaque.

Chapter 5

Discussion of Results

In monotonic loading, the plaque-thread materials tested here performed robustly and consistently, as shown in Figure 3.1. Agreement between samples from different mussels is particularly interesting considering the variability in material processing of these structures. Even among plaques deposited by the same individual mussel, protein polymorphism likely causes differences in plaque protein compositions [15]. Plaque size and proportions of plaque constituents (i.e. height of foamy core, thickness of cuticle) vary, and although the time between plaque deposition and collection was reasonably controlled, some plaques necessarily had longer exposure to seawater before collection than others. The mussel thus creates a strong material without controlling every material parameter at a minute level. In addition to reconciling material variability, the plaque-thread structure also accommodates internal damage and even partial delamination of the plaque from the substrate while maintaining its strength at large extensions.

In repeated loading, energy is dissipated as microscale tears and voids form within the disordered foam and the foam-thread interface experiences disruption. In some cases, a disc-shaped crack between the adhesive pad and substrate begins to propagate. The presence of such damage compromises small strain stiffness, but does not affect material

strength. A likely explanation for this insensitivity of strength to cyclic load history is an existence of multiple force transmission pathways between the thread and plaque-substrate interface. Another possibility is that mechanically induced chemical reactions within the plaque structure help to compensate for structural damage, as has been suggested to occur at the plaque interface [16]. These candidates may work in concert to deliver the observed robustness.

In nature, there is an upper limit to the force amplitudes that mussels regularly experience, and it has been argued that the plaque-thread structure is optimized to bear loads up to but not exceeding this value [17] [10]. The results presented here suggest that in addition to distributing load between an array of threads, the byssus evades failure by incorporating a multiplicity of structures capable of load-bearing. For example, multiple, nested sacrificial networks may exist within the structure, but are called to bear load only when needed. The incorporation of such fail-safe sacrificial or dissipative mechanisms would allow damage to be accommodated without catastrophic failure. The ability of the structure to maintain strength despite plaque-interface delamination could also suggest some ability of the chemical bonds at the interfaces to recover from previous damage, as in the antioxidant ability of Mfp-6 in plaque formation [18], and the subsequent maintenance of the reducing environment at the interface for many weeks [19]. This strategy of accommodation of microstructural damage is evident in other components of the mussel byssus: namely, the granular cuticle which surrounds both plaque and thread exhibits microcracking before catastrophic rupture [20].

Perhaps unsurprisingly, the mechanical behavior we observed shares character with measurements of the distal thread alone. The plaque accounts for only 10% of the total length of the plaque-thread structures tested, and is interpenetrated by the thread. The collagenous distal thread exhibits a high initial stiffness before yield, occurring at 10-20% strain, then a plateau and final stiffening beyond yield, in qualitative agreement

with our results [17]. In cyclic loading, the distal thread also exhibits stress softening and dissipative hysteresis that increases with increasing extension [6].

However, the recovery exhibited by distal thread contrasts with our results. In the thread, histidine-metal coordination bonds play a key role in determining mechanical response, and chelating metal from the byssal threads dramatically reduces their stiffness [21]. The disruption of metal coordination bonds is reversible, and the distal thread exhibits pH-dependent recovery of stiffness and length on the timescale of hours [21][6]. We do not observe appreciable recovery in small-strain stiffness at timescales up to 100 minutes, although previous work [8] (supporting) has shown 70% recovery of stiffness in identical conditions at a timescale of 24 hours. We do observe some level of immediate recovery, as we consistently find that in cyclic loading, progressive cycles result in higher forces than are observed at the same strain in the unloading of the previous cycle.

We do not see measurable recovery of small-strain stiffness (measured during loading) over longer timescales, suggesting that the stress softening in the distal thread differs from the softening evident in the plaque-thread. At large extensions, load transfer through the thread and plaque results in microstructural damage at the thread-foam interface. This damage, which occurs within the collagen fibers and the surrounding foam matrix, suggests a mechanical mismatch between the thread and foam core. Because damage to this thread-foam interface precedes damage detected at the cuticle-collagen matrix, it is likely that the thread-foam mismatch exceeds the mechanical mismatch between the cuticle and collagen, and that the cuticle-interior interface plays a larger role in load-bearing.

Manmade foams designed for structural applications are typically used in compression to enhance energy dissipation through controlled structural collapse, or to increase stiffness without substantially increasing mass [22]. In contrast, the foam within the mussel plaque is more likely subjected to tension and/or shear. The behavior of closed

cell polymeric foams in tension is dominated by bending of cell walls [23], which may occur in the larger, closed pores evident within the mussel plaque foam, but the role of the surrounding network of smaller, open pores is less clear [9]. Within the foam matrix, we observed crack propagation through pore centers suggesting that pore rupture can advance fracture. However, ductile or semi-ductile behavior within the foam matrix and matrix porosity could also contribute crack tip blunting, discouraging crack advance [24]. The disordered existence of heterogeneous material boundaries within the plaque-thread structure (between foam and water, or foam and thread, for example) may also reduce opportunities for linear crack advance, as has been proposed in another porous, non-mineralized biomaterial, squid sucker rings [25].

In the future, it will be useful to experimentally assess microstructural changes under loading in real time to distinguish these candidate mechanisms. Future measurement of plaque-specific properties, such as plaque porosity and foam modulus, coupled with computational studies, will better elucidate how void fraction, strut geometry, and material parameters contribute to energy dissipation in the plaque.

Chapter 6

Conclusion

The mussel plaque-thread structure leverages multiscale, multiphase structural components to support required loads even after damage occurs. As soft materials are increasingly candidates in multi-faceted functions, such as stretchable electronics, the design of materials with multiple routes to resiliency is essential. Translating this strategy to implement a multiplicity of load-bearing strategies in synthetic materials holds potential for creating new classes of soft, yet strong, architectured materials.

Appendix A

Modifications to Experimental Apparatus

A.1 Sample Preparation

Previous experiments testing samples with 1cm-2cm of exposed collagen thread have had success sandwiching the collagen thread between a piece of card stock sized approximately ∼2mm × 10mm and a piece of fine-grit sandpaper of the same size, then fixing the thread there with krazy (cyanoacrylate) glue.

In experiments with only 2mm of exposed thread, this cardstock-sandpaper sandwich became unwieldy, and I had more success gluing these samples to 1mm diameter glass rods. I did this by first arranging a small piece of cardstock underneath the thread. The glass rods as-sold are quite long, so I broke each rod into thirds, then dipped a section of the glass rod in a small puddle of glue, then set the glass rod on top of the thread. This way, the glue bonded to the thread and the piece of cardstock, but not the glass slide below. I found it useful to measure and cut dozens of cardstock pieces at once to streamline this process and ensure that the glass rods and cardstock pieces I used in each

experiment were close in size.

Gluing the threads to glass rods required a glue with more viscosity than krazy glue. I explored higher viscosity cyanoacrylate glues (Stew-Mac glues), epoxy (JB-kwik), and UV cure glues (Norland). In the end I found that a polyurethane glue (Gorilla glue) offered the best bond with the least spreading, although it required an overnight cure. The Norland glue spread only minimally, but the UV exposure completed dried the samples with the 10 minute cure, and I was not certain how the UV exposure would affect the thread's collagen. 5-minute epoxies are another candidate glue for experiments where an overnight cure is impractical.

A.2 Mechanical Fixtures

Previous experiments used a simple clamp closed by two small screws to hold samples during testing. Clamping a glass rod in this clamp proved to be precarious, so I designed a new clamp fixture to firmly hold the glass rod during testing. I envisioned a chuck that could simply be twisted to fasten the glass rod in place, which would also eliminate the step of screwing and unscrewing two tiny screws for each experiment.

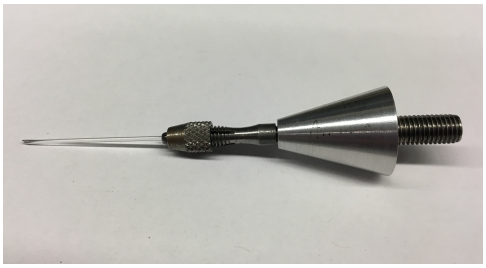

Figure A.1: The clamp fixture, shown with a glass rod held in its jaws.

The final fixture (Figure A.1) used a Small-Hole Drilling Adapter (McMaster-Carr 30505A5) as a chuck. UCSB's machine shop provided invaluable help in machining this

fixture, including opening the jaws slightly and attaching it to a collar for attachment to the tensile testing apparatus. To clamp the slide to the tensile testing apparatus, I

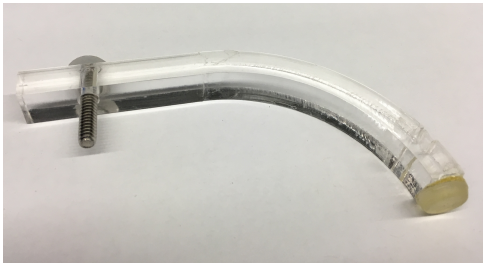

Figure A.2: The slide clamps, shown with a screw in the hole used to attach the clamp to the testing apparatus.

used slide clamps designed by Emma Filippidi (Figure A.2). These were laser-cut from acrylic. At one end, they accomodate screws for attachment to the apparatus, and at the other end their foot holds a glass slide firmly in place.

Figure A.3 shows a view of the entire testing apparatus.

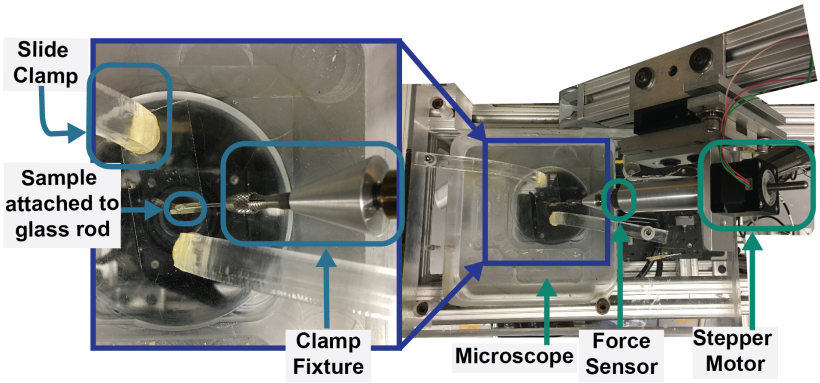

Figure A.3: The entire testing apparatus, shown from above. Inset shows a close up view of a slide with an adhered plaque, fixed to a glass rod and clamped for test. For clearer viewing, this sample is not hydrated.

A.3 Testing Apparatus Hardware

The tensile testing apparatus previously built [10] currently consists of a digital stepper motor (Haydon Switch and Instrument), an analog force sensor (Honeywell Model 31 Mid), and a microscope below the sample being tested. An in-line amplifier (Honeywell Model UV) amplifies the force sensor signal.

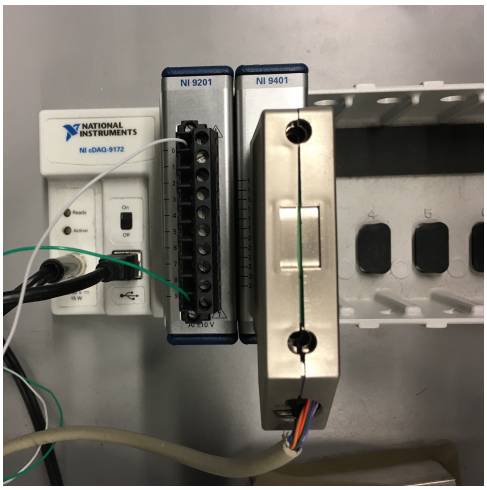

Figure A.4: The NI cDAQ 9172 interfaces with the stepper motor and force sensor. An NI 9201 card receives the analog signal from the force sensor while the NI 9401 card sends digital signals to control the stepper motor.

A National Instruments cDAQ-9172 (Figure A.4) is used to interface these elements with a benchtop computer. Previously, an NI PCIe-6321 was used, but it failed; the nature of its failure was never fully understood.

A.4 Testing Apparatus Software

The tensile testing apparatus previously built [10] is controlled by labVIEW programs. Because the three measuring components (the force sensor, stepper motor, and microscope) involve different signal types and different measurement frequencies, it is

useful to run them in the same labVIEW program, each within their own separate loop inside the main program. Attempts to combine these instruments into one global loop resulted in the entire program being run at the speed of the slowest instrument.

I found it useful to employ four different programs:

1. A microscope-only program that allowed me to align the microscope to the sample without collecting force/motor data (BottomCamera_Imager_MHW2.vi)

2. A program that only controlled the stepper motor and measured force to pre-load samples to a small initial load. This prevented me from performing entire experiments on samples which were clamped insufficiently to prevent sliding, or which had poorly bonded glass rods. (Initialize-to-F.vi)

3. A program that applied extension with the stepper motor, measured force, and imaged, then output labeled data files (.tiff and .xls) to the same folder. (Pull-To-Failure.vi, MultiCycle.vi, PulltoIntervalofYield-Stop.vi)

4. A motor-only program that allowed me to move the motor back to its initial position after an experiment. (MoveMotorDown.vi)

These programs are all backed up on the desktop of the benchtop computer next to the tensile testing machine.

Bibliography

[1] D. J. Crisp, G. Walker, G. A. Young, and A. B. Yule, *Adhesion and substrate choice in mussels and barnacles*, *Journal of Colloid and Interface Science* **104** (Mar., 1985) 40–50.

[2] N. Holten-Andersen, H. Zhao, and J. H. Waite, *Stiff Coatings on Compliant Biofibers*, *Biochemistry ACS* **48** (Mar., 2009) 2752–2759.

[3] J. H. Waite, *Nature's underwater adhesive specialist*, *International Journal of Adhesion and Adhesives* **7** (Jan., 1987) 9–14.

[4] L. M. McDowell, L. A. Burzio, J. H. Waite, and J. Schaefer, *Rotational Echo Double Resonance Detection of Cross-links Formed in Mussel Byssus under High-Flow Stress*, *Journal of Biological Chemistry* **274** (July, 1999) 20293–20295.

[5] B. P. Lee, P. Messersmith, J. Israelachvili, and J. Waite, *Mussel-Inspired Adhesives and Coatings*, *Annual Review of Materials Research* **41** (Aug., 2011) 99–132.

[6] E. Carrington and J. Gosline, *Mechanical design of mussel byssus: Load cycle and strain rate dependence*, *American Malacological Bulletin* **18** (2004), no. 1/2 135–142.

[7] C. Sun and J. H. Waite, *Mapping Chemical Gradients within and along a Fibrous Structural Tissue, Mussel Byssal Threads*, *Journal of Biological Chemistry* **280** (Nov., 2005) 39332–39336.

[8] C. N. Z. Schmitt, Y. Politi, A. Reinecke, and M. J. Harrington, *Role of Sacrificial ProteinMetal Bond Exchange in Mussel Byssal Thread Self-Healing*, *Biomacromolecules* (Aug., 2015) 150828095335001.

[9] E. Filippidi, D. G. DeMartini, P. Malo de Molina, E. W. Danner, J. Kim, M. E. Helgeson, J. H. Waite, and M. T. Valentine, *The microscopic network structure of mussel (Mytilus) adhesive plaques*, *Journal of The Royal Society Interface* **12** (Dec., 2015) 20150827.

[10] K. W. Desmond, N. A. Zacchia, J. H. Waite, and M. T. Valentine, *Dynamics of mussel plaque detachment*, *Soft Matter* (2015).

[11] M. W. Denny and R. T. Paine, *Celestial mechanics, sea-level changes, and intertidal ecology*, *The Biological Bulletin* **194** (1998), no. 2 108–115.

[12] E. Ducrot, Y. Chen, M. Bulters, R. P. Sijbesma, and C. Creton, *Toughening Elastomers with Sacrificial Bonds and Watching Them Break*, *Science* **344** (Apr., 2014) 186–189.

[13] R. E. Webber, C. Creton, H. R. Brown, and J. P. Gong, *Large Strain Hysteresis and Mullins Effect of Tough Double-Network Hydrogels*, *Macromolecules* **40** (Apr., 2007) 2919–2927.

[14] L. Mullins, *Softening of Rubber by Deformation*, *Rubber Chemistry and Technology* **42** (Mar., 1969) 339–362.

[15] S. C. Warner and J. H. Waite, *Expression of multiple forms of an adhesive plaque protein in an individual mussel, Mytilus edulis*, *Marine Biology* **134** (Sept., 1999) 729–734.

[16] J. H. Waite, *Mussel adhesion - the essential footwork*, *Journal of Experimental Biology* **in press**.

[17] E. C. Bell and J. M. Gosline, *Mechanical design of mussel byssus material yield enhances attachment strength*, *Journal of Experimental Biology* **199** (1996), no. 4 1005–1017.

[18] J. Yu, W. Wei, E. Danner, R. K. Ashley, J. N. Israelachvili, and J. H. Waite, *Mussel protein adhesion depends on interprotein thiol-mediated redox modulation*, *Nature Chemical Biology* **7** (July, 2011) 588–590.

[19] D. R. Miller, J. E. Spahn, and J. H. Waite, *The staying power of adhesion-associated antioxidant activity in Mytilus californianus*, *Journal of The Royal Society Interface* **12** (Oct., 2015) 20150614.

[20] N. Holten-Andersen, T. E. Mates, M. S. Toprak, G. D. Stucky, F. W. Zok, and J. H. Waite, *Metals and the Integrity of a Biological Coating: The Cuticle of Mussel Byssus*, *Langmuir* **25** (Mar., 2009) 3323–3326.

[21] M. J. Harrington and J. H. Waite, *Holdfast heroics: comparing the molecular and mechanical properties of Mytilus californianus byssal threads*, *Journal of Experimental Biology* **210** (Dec., 2007) 4307–4318.

[22] B. H. Smith, S. Szyniszewski, J. F. Hajjar, B. W. Schafer, and S. R. Arwade, *Steel foam for structures: A review of applications, manufacturing and material properties*, *Journal of Constructional Steel Research* **71** (Apr., 2012) 1–10.

[23] V. S. Deshpande and N. A. Fleck, *Multi-axial yield behaviour of polymer foams*, *Acta materialia* **49** (2001), no. 10 1859–1866.

[24] R. M. McMeeking, *Finite deformation analysis of crack-tip opening in elastic-plastic materials and implications for fracture*, *Journal of the Mechanics and Physics of Solids* **25** (Oct., 1977) 357–381.

[25] A. Miserez, J. C. Weaver, P. B. Pedersen, T. Schneeberk, R. T. Hanlon, D. Kisailus, and H. Birkedal, *Microstructural and Biochemical Characterization of the Nanoporous Sucker Rings from Dosidicus gigas*, *Advanced Materials* **21** (Jan., 2009) 401–406.